Research Article

Received: 16 February 2026 Revised: 5 May 2026 Published online in Wiley Online Library:

(wileyonlinelibrary.com) DOI 10.1002/pi.70155

Mechanically robust biochar-modified polystyrene foam with enhanced flame retardancy using halogen-free additives

Apurv Gaidhani, Harasavardanan Velumani Jayaraman, Stephan Edwards, Lauren Tribe and Paul Charpentier*

Abstract

Enhancing the fire safety of polystyrene (PS) insulation foams remains challenging due to their inherent flammability and environmental concerns associated with halogenated flame retardants. In this study, halogen-free flame-retardant PS foams are produced using a pilot-scale supercritical CO_2 extrusion process incorporating expandable graphite, melamine polyphosphate, biochar, and 10 wt% recycled PS. The optimized composite exhibits a refined cellular structure with the highest cell density (5.8×10^8 cells cm^{-3}) and the smallest average cell size (*ca* 50 μm). Transmission electron microscopy analysis confirms uniform dispersion of carbon-based fillers, providing effective heterogeneous nucleation sites, while rheological measurements indicate increased melt viscosity and elasticity, supporting stable cell growth. This engineered morphology results in a low thermal conductivity of 39 mW m^{-1} K^{-1} and enhanced load-bearing capability, with a specific compressive modulus of 74 MPa g^{-1} cm^3 and a specific compressive strength of 4.8 MPa g^{-1} cm^3. Flame-retardancy testing showed no melt dripping, rapid self-extinguishment within 12.5 s, and a limiting oxygen index of 25%. Char analysis indicated that biochar reinforces and densifies the expandable graphite–polyphosphate network, forming a compact protective layer. Overall, this work demonstrates a scalable, sustainable strategy for producing mechanically robust, halogen-free PS insulation foams under industrially relevant conditions.

Supporting information may be found in the online version of this article.

Keywords: polystyrene foam; biochar; halogen-free flame retardants; supercritical CO_2 extrusion; thermal insulation materials

INTRODUCTION

Polystyrene (PS) foams are widely used in building for insulation,[1] packaging,[2] automobile parts,[3] and home appliances because of their low density, thermal insulation capability, and processability.[4] Their relevance has increased significantly in recent years, particularly as the construction sector now accounts for approximately 30% of global final energy consumption.[5,6] Within this sector, space heating alone, which is an integral part of heating, ventilation, and air-conditioning systems, represents nearly 32–33% of total building energy use. Consequently, high-performance insulation materials are critical for reducing energy consumption and meeting decarbonization targets.[7]

Despite, their advantages, PS foams are heavily flammable: upon thermal degradation, the PS aromatic chain breaks and emits combustible volatile substances, shows melt dripping, and its porous nature further aggravates and spreads flame, releasing smoke.[8] Traditional halogenated flame retardants are useful at low dosages,[4,9] but their environmental concerns shifted interest to halogen-free flame retardants, focusing on intumescent systems comprising a protective char layer. Studies on expandable graphite (EG) and melamine polyphosphate (MPP) have attracted considerable interest recently; EG's expansion behavior forms a physical shield and MPP supports a phosphorus-rich char and thus mitigates flame.[1,10,11] Further, gases trapped in small cells of PS foam can also create a thermal barrier effect synergistic with EG to hinder polymer combustion.[12] Research has shown that phosphorus-based flame-retardant systems can enhance char formation, but they require high loadings to achieve the desired level of flame retardance. For example, mineral and phosphorus flame retardants in polyolefins often need to be incorporated at concentrations of 30 wt% or higher to achieve acceptable limiting oxygen index (LOI) or UL-94 ratings. However, such high dosages can compromise mechanical strength due to poor dispersion and agglomeration.[13] Similarly, aluminium polyphosphate-based intumescent systems in thermoplastics typically require more than 30 parts per hundred

* *Correspondence to: P Charpentier, Department of Chemical and Biochemical Engineering, University of Western Ontario, London, ON, N6A 5B9, Canada. E-mail: pcharpen@uwo.ca*

Department of Chemical and Biochemical Engineering, University of Western Ontario, London, ON, Canada

loading to produce a stable char and achieve meaningful reductions in heat release, highlighting their limited efficiency at lower dosages.[14] Out of all the halogen-free flame retardants, EG–MPP combination is widely studied,[1,9] though most of the reports are based on batch foaming, compression molding, or small-scale processing.

Global policies regarding sustainability and circular economy call for the use of recycled polymers, directly targeting PS foams in their regulatory framework.[15,16] Canada has a goal of 50% recycled content in packaging by 2030 and the European Union also targets to make all packaging to be reusable or recyclable by 2030, with ≥55% recycled content.[17] Such regulatory mandates transform PS foam from a sustainability preference into a compliance-driven necessity, motivating researchers to develop plastics that not only enable waste recovery and upcycling, but also enhance performance while maintaining product integrity. Recent advances have shown that designing controlled porous architectures in polymer systems can significantly influence mass transport, thermal behavior, and overall performance, underscoring the critical role of cell structure engineering in functional composites.[18–20] Biochar (BC), derived from waste biomass, has gained a lot of interest as a renewable filler for flame retardancy as it can strengthen the intumescent char and enhance heat stability.[21,22] Because of its porous structure, it can support mitigation of flammability, bringing in barrier effects.[23] Our previous studies demonstrated that BC acts as a multifunctional filler and a heterogeneous nucleating agent, thus leading to uniform pore structure as well as enhancing both the mechanical properties and the thermal insulation performance of PS foams.[24,25] BC has been widely reported as a promising flame-retardant additive, and its noncombustible and thermally stable nature can function as a heat-shielding barrier that limits heat transfer and protects the polymer matrix from thermal damage.[26,27] BC demonstrated good char reinforcement potential,[21,22] but its combined effect with EG and MPP in PS foam remains underreported, especially when the morphology and melt strength of foam are also influenced by additives. Adding BC along with recycled PS in foam production not only reduces the dependence on virgin polymer but also valorizes two waste streams.

Most of the previous studies on PS foams with carbon filler as additives relied on batch foaming or small-scale expansion methods, where PS is saturated with blowing agents and then expanded under certain experimental conditions, which does not consider the effect of shear force due to mixing, filler dispersion, uniformity, nucleation effect, and cell growth.[28] Some studies with EG and MPP showed that a 2:1 ratio of EG:MPP provided an effective flame-retardant synergy in PS systems due to the balance between intumescence and condensed-phase stabilization.[9,29] However, the simultaneous use of EG, MPP, and BC within a single formulation processed on a pilot-scale continuous extrusion line has not yet been explored. This represents a notable knowledge gap, as industrially relevant foaming conditions strongly influence the resulting foam morphology.

The objective of the work presented here was to develop and evaluate a halogen-free flame-retardant PS foam system incorporating EG, MPP, BC, and 10 wt% recycled PS, in alignment with sustainability and circular-economy goals. Four formulations were produced using a twin-screw continuous extrusion process coupled with supercritical CO_2 (sc-CO_2) foaming to examine the effects of these additives on foam expansion behavior, cellular morphology, thermal insulation performance, mechanical integrity, and flame retardancy. Transmission electron microscopy (TEM) and dynamic rheological analysis were conducted to evaluate filler dispersion and melt viscoelastic behavior, respectively. Thermal conductivity measurements and compression testing were carried out to assess insulation efficiency and structural robustness. Flame-retardant behavior was evaluated through propane torch vertical burning tests and LOI measurements, while thermal stability was assessed using thermogravimetric analysis (TGA) under air and nitrogen atmospheres. Char residue from vertical burning tests was analyzed using scanning electron microscopy (SEM) and Fourier transform infrared (FTIR) and Raman spectroscopies to elucidate the role of BC in the halogen-free flame-retardant system and to support the development of a flame-retardancy mechanism. Overall, the study aimed to advance the production of scalable, halogen-free, flame-retardant PS foams suitable for sustainable building insulation applications.

EXPERIMENTATION

Materials

BC, produced via pyrolysis of maple and oak sawdust, was kindly provided by Airex Energy (Quebec, Canada). PS (595T) with a melt flow index of 1.6 g (10 min)$^{-1}$ (200 °C, 5 kg) and a density of 1.04 g cm^{-3} was purchased from TotalEnergies Petrochemicals & Refining (USA). The blowing agent, CO_2 (99.9% purity), was supplied by Linde Canada. Talc powder (JetWhite 1HC, median particle size of 1.1 μm) was kindly donated by Magris Talc (USA). EG was kindly provided by Mei Wang Chemicals (Hangzhou, China) and had an average particle size of 80 μm with an expansion volume of 200 mL g^{-1}. MPP was also supplied by the same company, with a phosphorus content of 13.1%, nitrogen content of 41%, and a median particle size of 6 μm.

Extrusion foaming of PS composites

PS and composite foams were produced using a pilot-scale twin-screw extruder (Feininger SHJ-Z36 × 25, $D = 36$ mm, $L/D = 25$, throughput = 3 kg h^{-1}) coupled with a sc-CO_2 foaming system. All formulations contained 1 wt% talc as a nucleating agent and 10 wt% recycled PS foam to support circular-economy objectives. The detailed foam formulations and corresponding sample labels are provided in Table 1, and a schematic of the preparation steps

Table 1. Formulation details and sample labels for the PS composite foams prepared with halogen-free flame-retardant additives and recycled PS content

Sample label	PS (wt%)	EG (wt%)	MPP (wt%)	BC (wt%)	Recycled foam (%)	Talc (wt%)
Pristine PS	99	0	0	0	0	1
PS-BC-10R	86.5	0	0	2.5	10	1
PS-EG-MPP-10R	81.5	5	2.5	0	10	1
PS-EG-MPP-BC-10R	79	5	2.5	2.5	10	1

of extrusion foaming is shown in Fig. 1. Processing was carried out using a two-stage extrusion approach. In the primary extrusion stage, polymer melt mixing was performed at 190 °C (feed zone), 195 °C (compression zone), and 190 °C (metering zone). In the secondary extrusion stage, sc-CO_2 injection and cell nucleation occurred while the temperature profile was adjusted to 130, 195, and 165 °C, respectively, with the die temperature maintained at 140 °C. The system was operated at a screw speed of 50 rpm with sc-CO_2 injected at a pressure of 17.3 MPa, followed by ambient cooling of the extrudate. The reported pressure corresponds to the CO_2 injection pressure measured at the gas inlet port, located upstream near the feed section of the extruder. EG, MPP, and BC were mixed with PS pellets through dry blending prior to extrusion. In our previous work,[25] where BC was evaluated at 1, 2.5, 5, and 7.5 wt% loadings, 2.5 wt% BC was identified as the optimal concentration for achieving balanced cell morphology and thermal insulation performance. Therefore, BC was fixed at 2.5 wt% in the present formulations.

The formulation matrix used in this study was intentionally kept focused to isolate the principal roles of BC and the halogen-free intumescent system under industrially relevant foaming conditions. Pristine PS was used as the baseline control, PS-BC-10R was selected to evaluate the independent effect of BC on cellular morphology and composite performance, PS-EG-MPP-10R was used to establish the flame-retardant contribution of the binary intumescent system, and PS-EG-MPP-BC-10R was designed to determine whether BC could further improve the EG–MPP system through char reinforcement and morphology control. Thus, the selected formulations were intended as a hypothesis-driven comparative set rather than a broad formulation-screening study. The additive levels were selected based on both literature precedent and prior optimization studies. The BC loading was fixed at 2.5 wt% as our previous work identified this concentration as optimal for improving cell morphology and thermal insulation without adversely affecting foamability. The EG:MPP ratio was fixed at 2:1 based on previous reports of PS systems showing that this ratio provides an effective balance between intumescent expansion and condensed-phase char stabilization.[9] The total EG/MPP loading was limited to maintain processability and stable extrusion foaming under pilot-scale conditions, while 10 wt% recycled PS was selected as a practical incorporation level that supports sustainability goals without destabilizing the foaming process.

Characterization

Foam density was determined according to ASTM D1622. Three rectangular specimens (23 × 8 × 7 mm^3) were tested per formulation, and the average value is reported. The foam skin was removed prior to measurement. Expansion ratio of foam (ϕ) was calculated as[30]:

$$\phi = \frac{\rho_{solid}}{\rho_{foam}} \quad (1)$$

where ρ_{solid} is the bulk density of the solid polymer composite and ρ_{foam} is the density of the foam.

Foam morphology was analyzed using SEM (Hitachi FlexSEM 1000 II) at an accelerating voltage of 5 kV. Samples were freeze-fractured in liquid nitrogen, the skin was removed, and observations were made perpendicular to the extrusion direction at the foam center. Cell size and particle analysis were performed using Fiji (ImageJ) from SEM micrographs (×50). Cell size was defined as the average diameter of all cells within an image. Cell size was

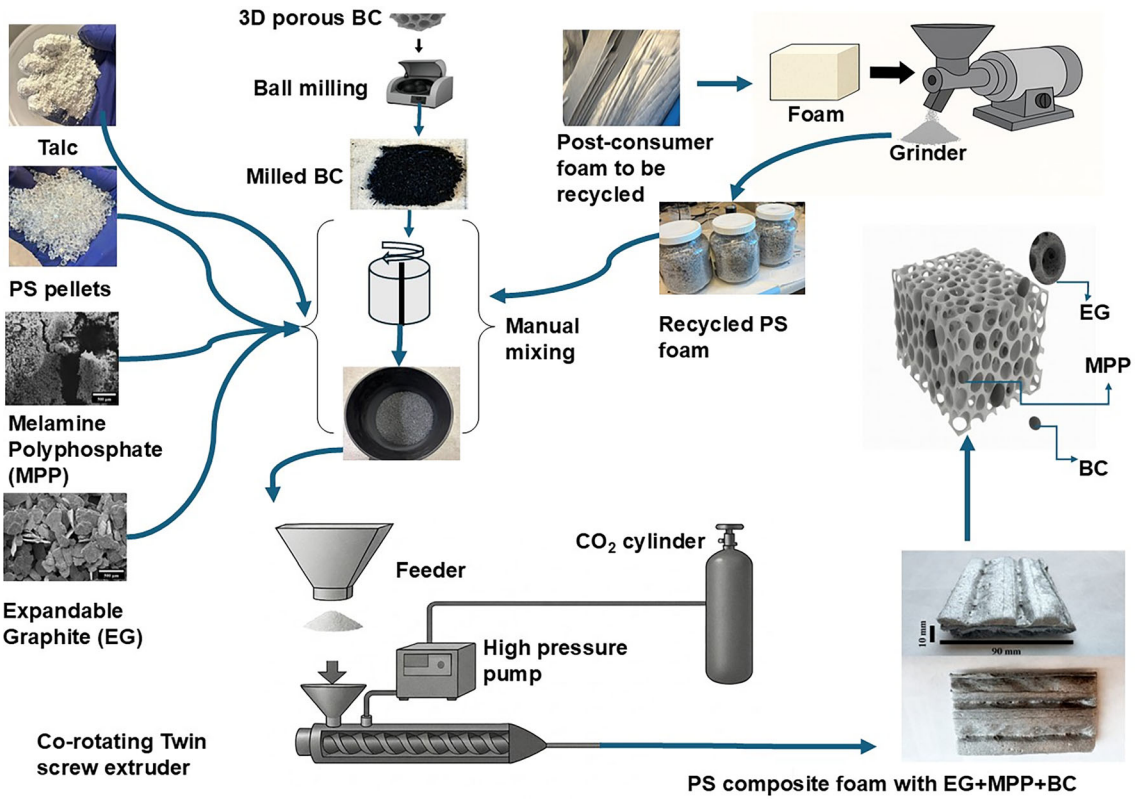

Figure 1. Two-step preparation process of flame-retardant PS composite foam: manual mixing followed by twin-screw foaming extrusion.

Polymer International published by John Wiley & Sons Ltd on behalf of Society of Chemical Industry.

determined by calculating the equivalent circular diameter from the projected area of each cell. This method enables consistent statistical analysis of irregular cell geometries. Cell density (N_0) was calculated as[31]:

$$N_0 = \left(\frac{n}{A}\right)^{3/2} \phi \quad (2)$$

where n is the number of cells in a SEM image, A is the area of the SEM image and N_0 is the number of cells per unit volume. Cell size distributions were plotted using histograms and Gaussian fitting.

For TEM analysis, foam samples were embedded in Spurr's epoxy resin and polymerized overnight at 60 °C. Ultrathin sections were prepared using a Leica UCT ultramicrotome and collected on copper grids. The sections were examined using a JEOL JEM 1230 microscope (JEOL, Peabody, MA, USA) operating at an accelerating voltage of 80 kV. Images were acquired using a 4-megapixel digital camera (Advanced Microscopy Techniques, Woburn, MA, USA).

The rheological behavior of the polymer formulation was characterized using a Discovery Hybrid Rheometer, HR 20 series rheometer with a parallel plate geometry (TA Instruments, Delaware, USA). Here the parallel plates were set to a temperature of 180 °C. Disc-shaped specimens (25 mm in diameter × 0.2 mm in thickness) were compression-molded at 180 °C and 1500 psi for 10 min. The storage and loss moduli (G' and G'', respectively) were measured by performing dynamic frequency sweeps using a 25 mm parallel-plate fixture at a 0.1% strain amplitude and a frequency range from 100.0 to 0.1 rad s^{-1}. The test temperature was selected based on preliminary trials (170–200 °C), where lower temperatures resulted in insufficient melt relaxation and higher temperatures led to time-dependent drift in rheological properties; thus, 180 °C provided stable and reproducible measurements. The strain amplitude was chosen within the linear viscoelastic region as determined from amplitude sweep analysis.

Thermal conductivity measurements were performed using a heat flow meter apparatus (Fox 200, TA Instruments, LaserComp) under steady-state conditions. Square specimens with dimensions of 200 × 200 mm^2 were used for all measurements. Prior to recording data, a stabilization period of approximately 5 min was allowed to ensure steady-state heat flow conditions, and each test was conducted for a total duration of approximately 45 min. The reported values represent the average of three measurements. TGA (Q600, TA Instruments, USA) was conducted from room temperature to 900 °C at 10 °C min^{-1} under nitrogen and air (100 mL min^{-1}). TGA and derivative thermogravimetric (DTG) curves were used to evaluate mass retention and decomposition behavior. Compressive properties were measured following ASTM D1621 using an Instron 5943 with a 1 kN load cell. Seven specimens (16 × 16 × 7 mm^3) were tested per formulation. A 2 N preload ensured uniform contact, and compression was performed at 0.7 mm min^{-1} up to 50% strain. Compressive modulus was obtained from the initial linear region, and strength was defined at 10% strain. Specific properties were calculated by normalizing with foam density. Reduced thickness was necessitated by extrudate dimensions. All foam specimens used for mechanical and thermal characterization were prepared after removal of the outer skin layer, and measurements were conducted on the core region to ensure representative bulk foam properties.

Flame retardancy was evaluated using vertical burning and LOI tests. Vertical burning followed UL-94 procedures except that a propane flame was used. The blue flame was approximately 20 mm in length, with an overall flame height of *ca* 40 mm. The specimen was positioned such that the flame was applied at a distance of approximately 10 mm from the lower edge of the sample (specimen size: 127 × 12.7 × 6 mm^3), consistent with standard UL-94 test geometry. Each specimen was exposed to the flame for *ca* 10 s, followed by reignition to assess repeatability. All tests were conducted under identical conditions to ensure consistency. LOI tests (ASTM D2863) were conducted using a QINSUN-F101D tester on specimens (120 × 6.5 × 6 mm^3). Three specimens per formulation were tested and the results were averaged. For flame-retardancy testing, specimens were tested with the as-extruded skin intact.

Morphological and structural analyses of fillers (EG, MPP, BC) and char residues were performed using SEM, FTIR spectroscopy and Raman spectroscopy as applicable. Samples were mounted on conductive carbon tape and cleaned by gentle air blowing. SEM micrographs (×50) were processed using Fiji (ImageJ). FTIR spectra (Nicolet 6700, Thermo Scientific) were collected for BC and char residues over 600–4000 cm^{-1}. Raman spectra (RXNI-785, Kaiser Optical Systems, USA; 785 nm excitation) were acquired for BC and char residues to assess graphitic ordering.

RESULTS AND DISCUSSION

Extrusion foaming process under high filler loading

Foaming PS at total filler contents approaching 11 wt% (EG, MPP, BC, and talc) presents substantial challenges due to increased melt viscosity, reduced flowability, and the tendency of particles to disrupt gas dissolution and cell growth. In this study, stable foaming was achieved on a pilot-scale twin-screw extruder using sc-CO_2 at 17.3 MPa, a pressure identified through trial-and-error optimization to ensure complete gas dissolution and suppress premature nucleation within the barrel, which resulted in optimized cell morphology and expansion ratio. Careful temperature control maintained the melt viscosity within a workable range that allowed efficient mixing while preserving the melt strength required for cell stabilization. The extruder was purged after every formulation to prevent filler accumulation and maintain consistent processing.

The high-pressure CO_2 enabled the formation of a homogeneous polymer–gas solution, while avoiding abrupt pressure drops along the screw prevented pre-foaming, an issue commonly observed at high filler loadings due to increased internal friction and localized flow resistance. Uniform filler dispersion and controlled rheology helped minimize filler agglomeration, which can otherwise trigger cell coalescence and irregular foam morphology. Cell nucleation was predominantly initiated at the die exit during the rapid pressure drop, allowing controlled growth and expansion despite the heavy filler content. Overall, the combination of optimized pressure, temperature profile, and mixing conditions enabled reliable pilot-scale foaming and demonstrated the feasibility of producing halogen-free, flame-retardant PS foams with high inorganic and carbonaceous additive loadings.

Foam microstructure and cellular morphology

Figure 2 presents the SEM micrographs and corresponding cell-size distributions of pristine PS and of the composite foams. Pristine PS exhibits large, irregular cells with relatively smooth walls (Fig. 2(a1),(a2)), characteristic of low nucleation density in unfilled polymers. The addition of 10 wt% recycled PS and 2.5 wt% BC yielded markedly smaller and more uniform cellular structures

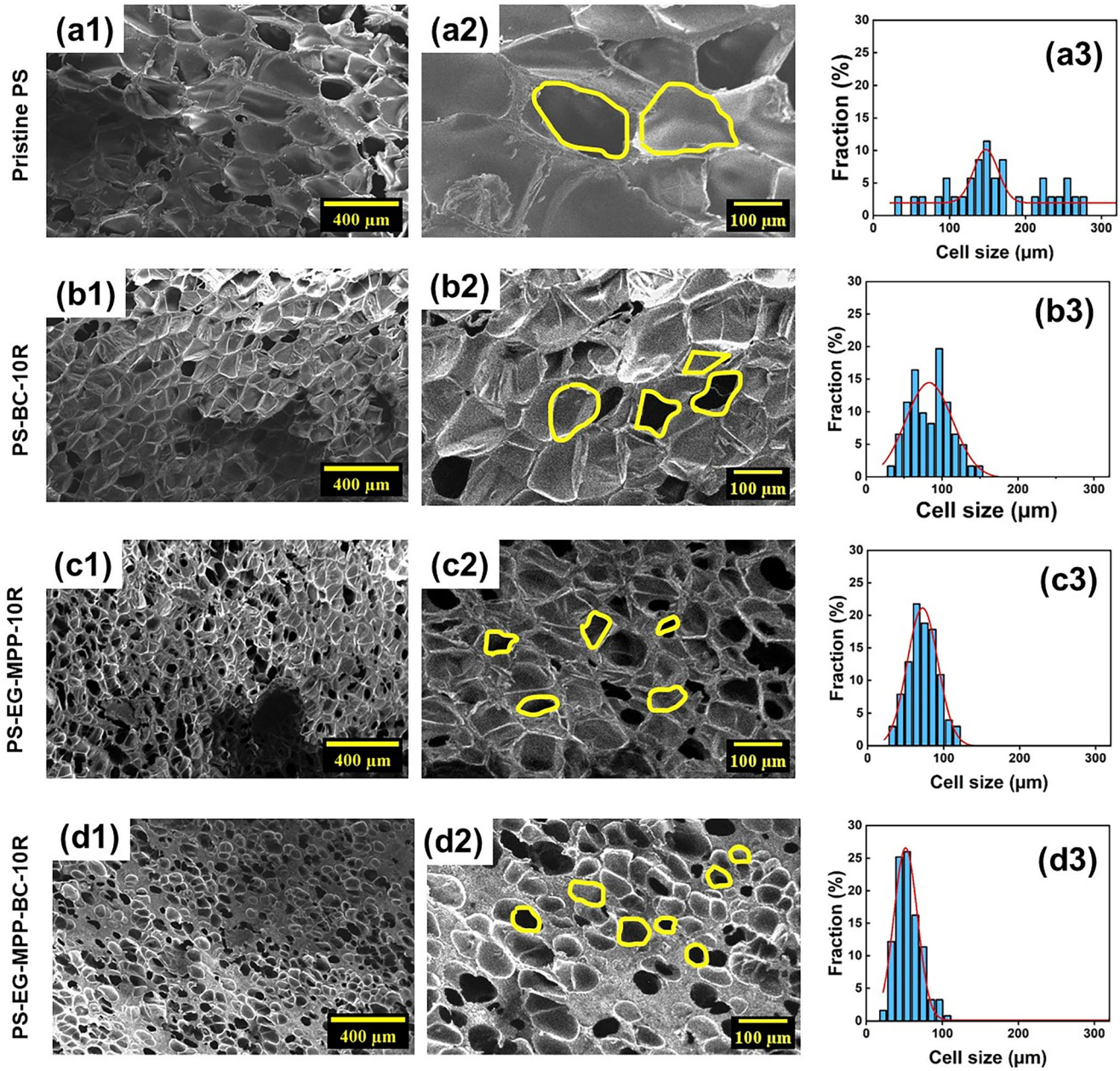

Figure 2. SEM micrographs of (a1, a2) pristine PS, (b1, b2) PS-BC-10R, (c1, c2) PS-EG-MPP-10R, and (d1, d2) PS-EG-MPP-BC-10R foams at low and high magnifications, showing the effect of BC, EG, and MPP on cell nucleation and morphology (yellow outlines represent cells).

(Fig. 2(b1),(b2)), confirming the strong nucleating effect of carbonaceous micro- and nanodomains within BC. When EG and MPP are incorporated (Fig. 2(c1)–(d2)), the cell morphology becomes even smaller, demonstrating the combined heterogeneous nucleation effects of EG platelets and BC particles. EG, with its large aspect ratio and abundant edge sites, provides effective heterogeneous nucleation sites,[32,33] whereas BC contributes graphitic microsurfaces and oxygen-containing functional groups that lower the energy barrier for bubble initiation.[34,35] As a result, the composite foams show narrower cell-size distributions (Fig. 2(b3),(c3),(d3)) as well as significantly reduced average cell sizes relative to pristine PS. The PS-EG-MPP-BC-10R formulation exhibited smallest cells and highest uniformity, indicating a strong cooperative effect among the three solid fillers. These results confirm that, despite the high overall filler loading, proper dispersion and CO_2 dissolution management within the melt can enable stable and consistent cell nucleation.

Figure 3 quantifies the microstructural characteristics derived from the SEM images, including average cell size, cell density, and expansion ratio. Pristine PS exhibited the largest cell size and lowest cell density (Fig. 3(a),(b)), reflecting its limited intrinsic nucleating ability. Incorporation of BC (PS-BC-10R) reduced cell size by more than half and increased cell density nearly fourfold, confirming the nucleating efficiency of BC previously observed for carbon fillers.[34] When EG and MPP were introduced (PS-EG-MPP-10R and PS-EG-MPP-BC-10R), cell size decreased further and cell density increased, indicating that these additives also contribute nucleation sites through their surface topology. The

Polymer International published by John Wiley & Sons Ltd on behalf of Society of Chemical Industry.

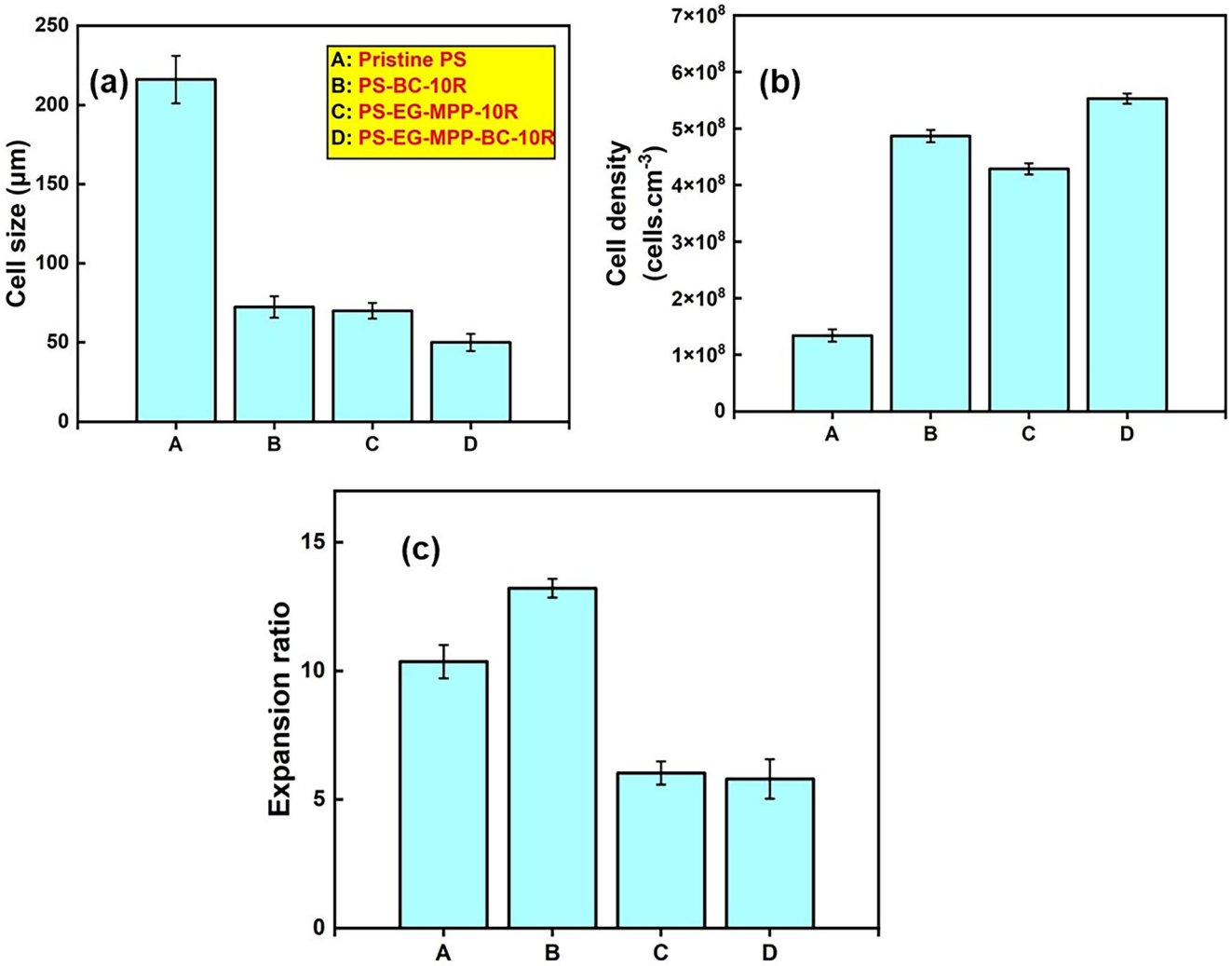

Figure. 3. Quantitative foam morphology parameters for pristine PS (A), PS-BC-10R (B), PS-EG-MPP-10R (C), and PS-EG-MPP-BC-10R (D): (a) average cell size, (b) cell density, and (c) expansion ratio.

multifiller formulation (PS-EG-MPP-BC-10R) produced the smallest cells and highest cell density, demonstrating a combined influence of EG, MPP, and BC on bubble nucleation. Enhanced nucleation, however, was accompanied by increased apparent foam density at high additive loading (*ca* 11 wt%). Elevated melt viscosity and restricted gas mobility limited bubble growth, reducing the expansion ratio (Fig. 3(c)), consistent with highly filled polymer foams where improved nucleation competes with constrained cell expansion.[36,37] Despite this trade-off, the foams remained homogeneous and stable, indicating that the optimized sc-CO_2 pressure (17.3 MPa) was sufficient to sustain steady-state foaming. Overall, EG, MPP, and BC effectively refined the cellular structure under industrially relevant conditions, supporting the development of halogen-free PS foams with improved performance.

TEM analysis was performed to evaluate the dispersion of fillers within the PS matrix and their influence on foaming behavior (Fig. 4). In PS-BC-10R (Fig. 4(a)) and PS-EG-MPP-BC-10R (Fig. 4(c)), carbon-based fillers (BC and/or EG, highlighted by yellow arrows) are relatively well dispersed within the matrix. In contrast, PS-EG-MPP-10R (Fig. 4(b)) shows comparatively less uniform dispersion due to lower detected presence of carbon fillers. Notably, carbon particles are frequently observed at or near the cell walls, which could indicate their role as preferential sites for heterogeneous nucleation during the early stages of bubble formation. The improved dispersion of carbon fillers possibly could have provided a higher number of effective heterogeneous nucleation sites, which correlated with the observed increase in cell density (Fig. 3(b)). This indicates that better filler dispersion promotes nucleation during foaming, resulting in smaller and more uniform cellular structures. These observations support the role of carbon fillers in enhancing foam morphology through nucleation control.

Rheological behavior of PS composites

The rheological properties of polymer melts play a critical role in foam nucleation, growth, and stabilization, particularly through their influence on melt strength and viscoelastic response.[38,39] The rheological behavior of the PS composites was investigated to understand the influence of fillers on melt viscoelasticity and its implications for foaming behavior. Figure 5 shows the variation of storage modulus (G'), loss modulus (G''), tan δ, and complex viscosity (η^*) as a function of angular frequency.

The pristine PS exhibits typical shear-thinning behavior, with both G' and G'' increasing with frequency. At low frequencies,

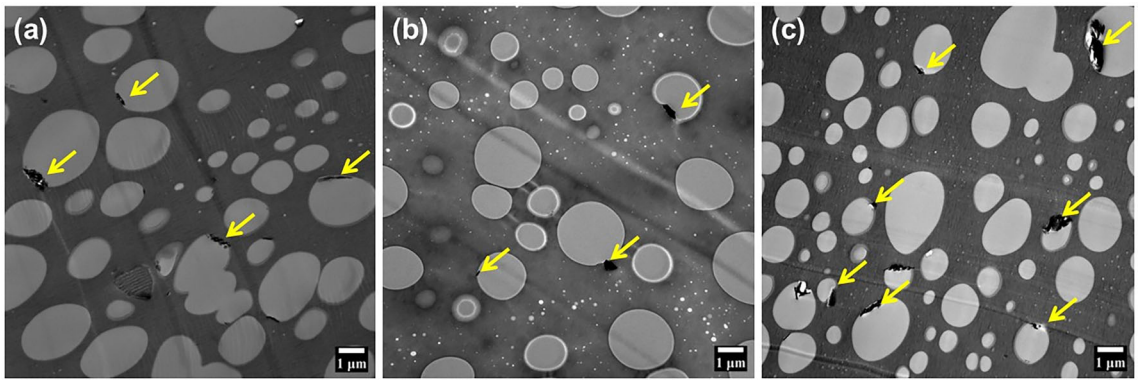

Figure 4. TEM images showing dispersion of fillers in PS composites: (a) PS-BC-10R, (b) PS-EG-MPP-10R, and (c) PS-EG-MPP-BC-10R (yellow arrows indicate the presence of carbon fillers).

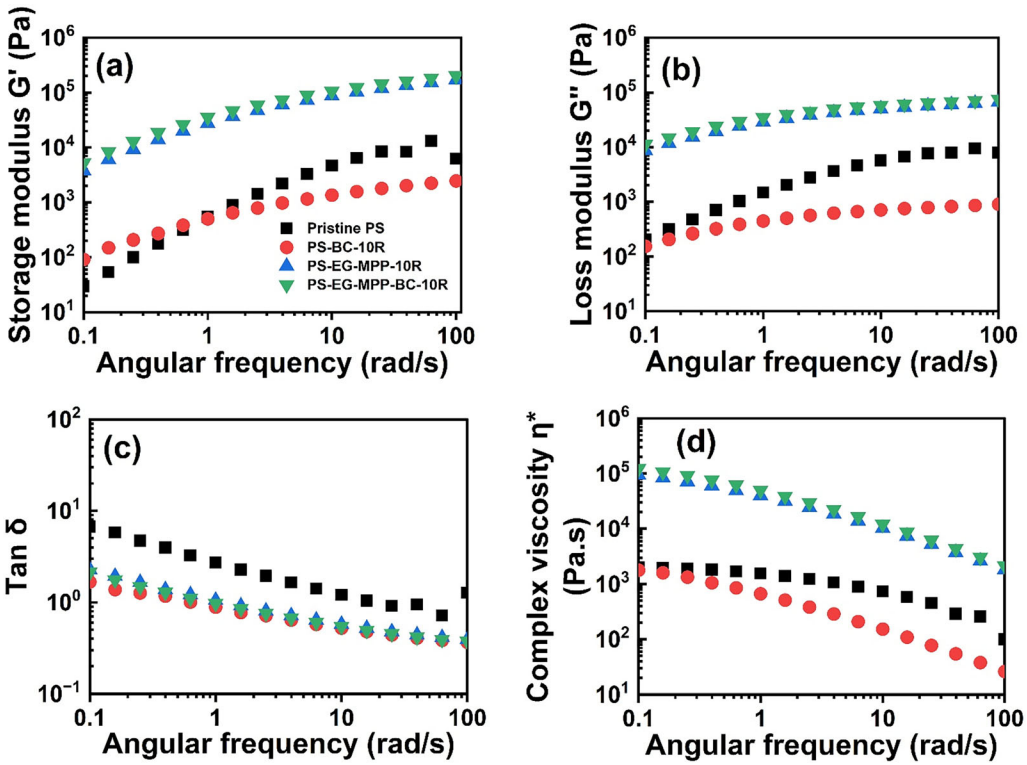

Figure 5. Frequency-dependent rheological behavior of PS composites: (a) storage modulus G', (b) loss modulus G'', (c) tan δ, and (d) complex viscosity η^*.

tan δ values are greater than unity, indicating a dominant viscous response, whereas at higher frequencies, the viscoelastic response shifts toward a more elastic behavior. The incorporation of BC (PS-BC-10R) results in a slight reduction in both storage modulus and complex viscosity compared to pristine PS, suggesting a modest decrease in melt resistance to deformation. This behavior may be attributed to the limited reinforcement effect and possible disruption of chain entanglements at low BC loading. In contrast, the addition of EG and MPP (PS-EG-MPP-10R) significantly increases both G' and η^*, particularly at low frequencies, indicating enhanced melt elasticity and resistance to flow. This effect becomes more pronounced in the multifiller system (PS-EG-MPP-BC-10R), where the highest storage modulus and complex viscosity are observed across the entire frequency range. The reduced frequency dependence of G' in these systems suggests restricted polymer chain mobility due to the presence of solid fillers and potential formation of a weak filler network. The decrease in tan δ for EG- and MPP-containing systems further indicates a shift toward more elastic behavior, although the composites still exhibit predominantly viscoelastic liquid characteristics. The increased melt viscosity and elasticity in these formulations influenced foaming behavior by enhancing melt strength, which supported cell stability during growth, while simultaneously limiting cell expansion at high filler loadings.[40]

Polymer International published by John Wiley & Sons Ltd on behalf of Society of Chemical Industry.

Overall, these results demonstrate that the combined incorporation of EG, MPP, and BC significantly modifies the rheological response of PS, leading to increased melt strength and elasticity, which play a critical role in controlling foam morphology and expansion behavior.

Thermal conductivity and mechanical properties

Figure 6(a) presents the thermal conductivity of the four PS foam formulations relative to pristine PS (*ca* 38 mW m^{-1} K^{-1}). The PS-BC-10R sample exhibited a noticeable reduction in thermal conductivity (*ca* 33 mW m^{-1} K^{-1}), likely due to the inherently low thermal conductivity of BC and its ability to disrupt heat transfer through its porous carbon structure.[41] In contrast, the foams containing EG and MPP showed thermal conductivities that remained comparable to that of pristine PS (*ca* 37.5 mW m^{-1} K^{-1} for PS-EG-MPP-10R and *ca* 39 mW m^{-1} K^{-1} for PS-EG-MPP-BC-10R). The slight increase is attributed to localized conductive pathways formed by graphite flakes at higher loadings (*ca* 5 wt% EG).[42,43] Despite this effect, all foams remain within the insulation-grade range. Notably, PS-EG-MPP-BC-10R maintains conductivity close to that of pristine PS while offering improved flame retardancy.

Figure 6(b) shows the characteristic compressive stress–strain response of closed-cell foams: an initial elastic region (*ca* 8–10% strain), a plateau region dominated by cell collapse, and a densification region. Pristine PS displayed the lowest stresses, consistent with its larger cells and thinner walls. BC addition produced only modest stiffening. In contrast, EG- and MPP-containing foams (samples C and D) exhibited markedly higher compressive stress at 10% strain (over threefold higher than pristine PS), reflecting thicker cell walls and increased solid fraction (*ca* 11 wt% additives). PS-EG-MPP-BC-10R showed the highest resistance, indicating cooperative reinforcement.

The compressive modulus and specific compressive modulus results are shown in Fig. 6(c). The compressive modulus exhibited a clear increasing trend from pristine PS (*ca* 3 MPa) to PS-BC-10R (*ca* 3.5 MPa), PS-EG-MPP-10R (*ca* 10 MPa), and PS-EG-MPP-BC-10R (*ca* 15 MPa). After density normalization, the specific modulus rose from *ca* 30 (A) to *ca* 40 (B), *ca* 55 (C), and *ca* 74 MPa g^{-1} cm^3 (D), indicating that stiffness gains arise from both density and improved stress transfer. The PS-EG-MPP-BC-10R formulation achieved more than a 2.4-fold enhancement in specific modulus over pristine PS. Figure 4(d) shows that the compressive strength and specific compressive strength follow the same progressive improvement. While pristine PS exhibited a compressive strength of *ca* 0.3 MPa, PS-EG-MPP-10R (sample C) reached *ca* 0.83 MPa and PS-EG-MPP-BC-10R (sample D) reached *ca* 0.88 MPa. When

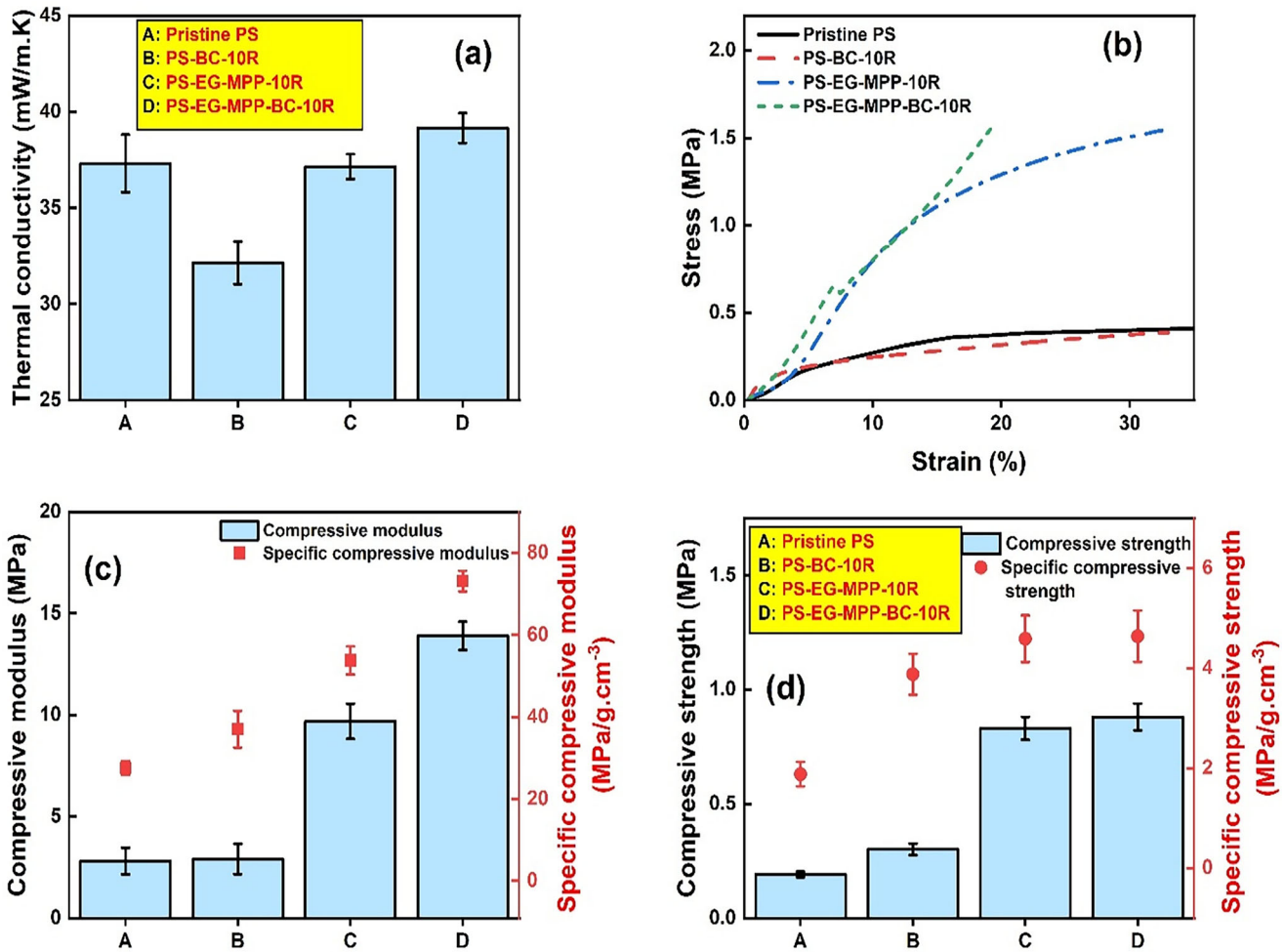

Figure 6. Thermal and mechanical performance of pristine PS (A), PS-BC-10R (B), PS-EG-MPP-10R (C), and PS-EG-MPP-BC-10R (D): (a) thermal conductivity; (b) compressive stress–strain curves under quasi-static loading; (c) compressive modulus and specific compressive modulus; and (d) compressive strength and specific compressive strength.

normalized by density, the specific compressive strength for samples C and D (*ca* 4.5–4.7 MPa g^{-1} cm^3) was approximately 2.7 times higher than that of pristine PS (*ca* 1.8 MPa g^{-1} cm^3). Notably, samples C and D exhibited similar specific compressive strength values, suggesting that EG and MPP predominantly govern the strengthening effect, while BC contributes additional reinforcement without compromising foamability. The enhanced compression performance of PS-EG-MPP-BC-10R is attributed to its refined cellular structure and hybrid filler network. Higher cell density and smaller cell size promote more effective stress distribution, while EG, MPP, and BC increase cell-wall stiffness.[44,45] Overall, the PS-EG-MPP-BC-10R foam demonstrates a favorable balance of insulation capability and mechanical robustness, supporting its potential for halogen-free, biocomposite building insulation applications.

Thermal degradation behavior

TGA was used to examine the thermal degradation behavior of pristine PS and the PS composite foam formulations under N_2 and air atmospheres. TGA and DTG curves are presented in Fig. 7. The thermal degradation parameters obtained from TGA for pristine PS and PS composites under N_2 and air atmospheres are presented in Table 2. Under N_2 atmosphere (Fig. 7(a),(b)), pristine PS exhibited a single-step degradation profile with an onset temperature ($T_{5\%}$) of 376.4 °C, T_{max} of 412.1 °C, minimal char yield (*ca* 2.1–2.5 wt%), and the highest mass-loss rate at T_{max} (−3.1% °C^{-1}), indicating rapid volatilization and negligible condensed-phase stabilization.[46] The incorporation of BC (PS-BC-10R) shifted $T_{5\%}$ to a higher temperature (382.7 °C) and increased char formation to *ca* 6.4–6.9 wt%, while reducing the degradation rate (−2.5% °C^{-1}), reflecting the physical barrier and carbon residue contributions of BC.[47] PS-EG-MPP-10R showed a comparable T_{max} (418.0 °C) and a moderate char yield (*ca* 2.8–3.4 wt%), attributed to MPP-induced char promotion and EG-related barrier effects,[48] together with a lowered mass-loss rate at T_{max} (−2.3% °C^{-1}). The ternary formulation PS-EG-MPP-BC-10R displayed the most pronounced improvement relative to pristine PS, combining a higher T_{max} (419.7 °C) with the largest char residues across 500–700 °C (8.4–10.8 wt%) and the lowest degradation rate among the composites (−2.2% °C^{-1}). These results demonstrate a

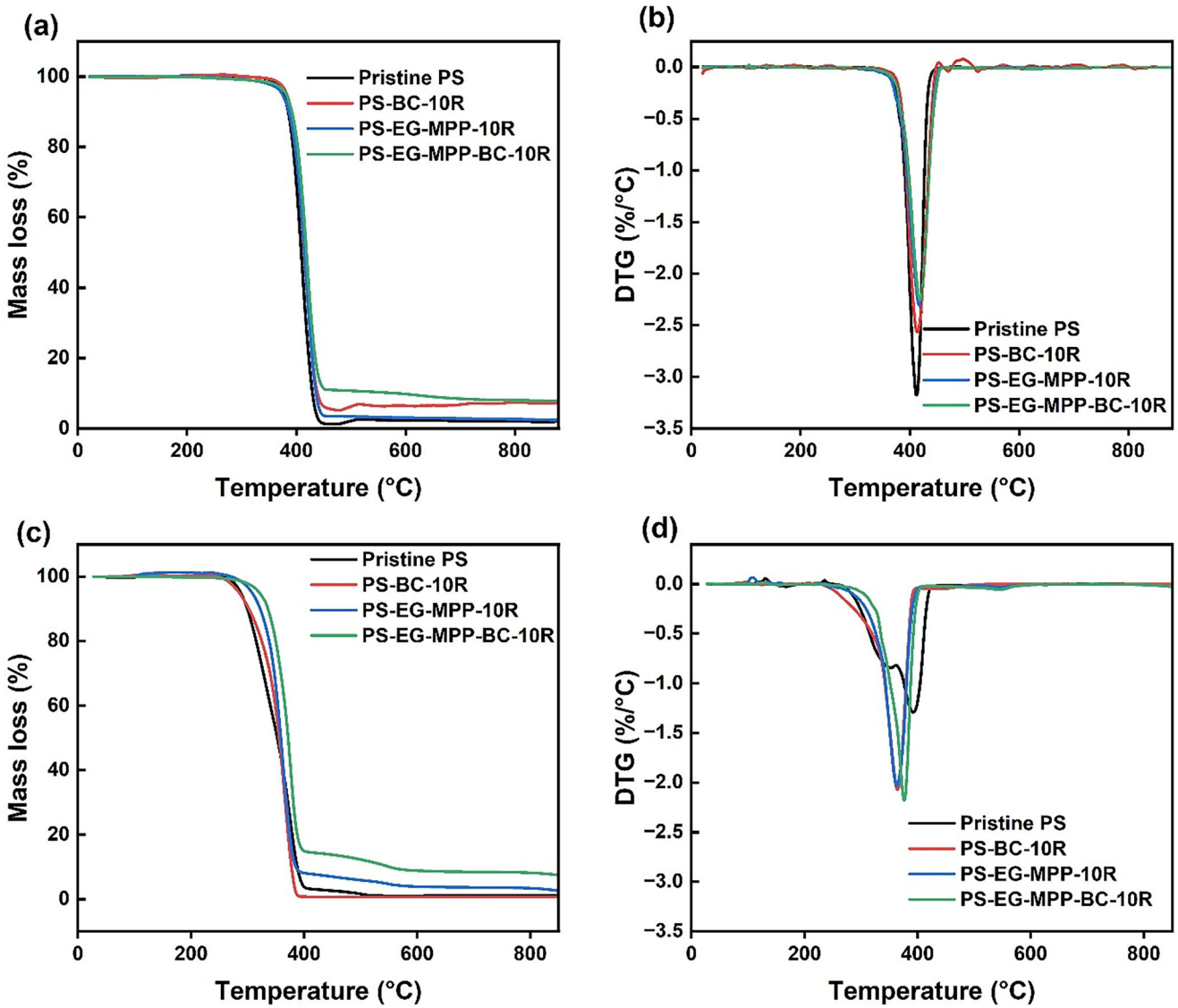

Figure 7. TGA and DTG curves of pristine PS and flame-retardant composites: (a, b) N_2 atmosphere; (c, d) air atmosphere.

Table 2. TGA and DTG data of pristine and fire-retardant PS composite foams under N_2 and air atmospheres

Sample	Atmosphere	$T_{5\%}$ (°C)	$T_{50\%}$ (°C)	T_{max} (°C)	Char residue (wt%) 500 °C	600 °C	700 °C	Mass loss rate at T_{max} (% °C^{-1})
Pristine PS	N_2	376.4	408.7	412.1	2.5	2.3	2.1	−3.1
	Air	286.7	351.8	385.6	2.3	2.1	2.0	−1.3
PS-BC-10R	N_2	382.7	414.1	413.8	6.9	6.4	6.5	−2.5
	Air	284.4	358.4	362.5	0.7	0.7	0.7	−2.0
PS-EG-MPP-10R	N_2	373.6	414.6	418	3.4	3.1	2.8	−2.3
	Air	306.7	358.5	361.4	5.9	3.9	3.6	−2.0
PS-EG-MPP-BC-10R	N_2	381.5	418.3	419.7	10.8	9.8	8.4	−2.2
	Air	320.6	371.5	374.9	12.3	8.8	8.5	−2.2

$T_{5\%}$ and $T_{50\%}$ represent the temperatures at 5% and 50% mass loss, respectively, while T_{max} corresponds to the temperature at the maximum decomposition rate (DTG peak).

combined condensed-phase mechanism, where EG expansion, MPP-driven intumescence, and BC-derived carbon reinforcement collectively stabilized decomposition and enhanced thermal resistance under inert conditions.

In oxidative conditions (Fig. 7(c),(d)), pristine PS degraded earlier than for the N_2 atmosphere ($T_{5\%}$ = 286.7 °C) with a lower T_{max} (385.6 °C) and negligible protective residue (*ca* 2.0–2.3 wt%), accompanied by a reduced, but still sharp degradation peak (−1.3% °C^{-1}), consistent with unprotected oxidative volatilization. Liu *et al.*[49] also observed that the temperatures for peak mass-loss rate for PS and its composites were lower for air atmosphere than for N_2 atmosphere due to the presence of oxygen accelerating the degradation of polymers. PS-BC-10R did not significantly improve onset stability ($T_{5\%}$ = 284.4 °C) and yielded minimal char (<1 wt%), reflecting partial oxidation of the BC residue. In contrast, PS-EG-MPP-10R showed markedly delayed degradation with a higher $T_{5\%}$ (306.7 °C), increased char retention (*ca* 3.6–5.9 wt%), and moderate mass-loss rate (−2.0% °C^{-1}), evidencing the formation of an intumescent, protective layer supported by EG expansion. The PS-EG-MPP-BC-10R system delivered the highest flame-retardant performance, exhibiting the most significant shift in thermal stability ($T_{5\%}$ = 320.6 °C; T_{max} = 374.9 °C), the greatest char residues (8.5–12.3 wt%), and sustained suppression of mass loss (−2.2% °C^{-1}).

Flame retardancy performance

The flame retardancy of the PS composite foams was evaluated using torch vertical burning tests and LOI measurements. The torch vertical burning test using a propane flame has been widely adopted in previous literature as a practical screening method for evaluating the flame retardancy of PS-based insulation materials.[50–52] During the torch vertical burning tests, corresponding burning behaviors were recorded as videos.

Table 3 lists the results of the torch vertical burning test and LOI test of PS and its fire-retardant composite foam. Figure 8 presents digital images of torch vertical burning tests for PS composite foams and conventional PS foam insulation materials.

As expected, pristine PS exhibited rapid ignition and sustained burning without char formation, accompanied by extensive molten dripping throughout flame exposure.[53,54] The specimen was completely burnt in less than 20 s after flame removal with extensive dripping and showed no tendency to self-extinguish, consistent with its low LOI value (18%). PS-BC-10R demonstrated a similar burning behavior to pristine PS, characterized by continued flame propagation, substantial dripping, and no self-extinguishing response, despite a slight increase in LOI (20%). These observations indicated that BC alone was insufficient to impart significant flame retardancy under direct flame impingement, as its carbon framework could not independently generate a coherent protective barrier or suppress melt flow during combustion. In contrast, PS-EG-MPP-10R exhibited clear improvements relative to pristine PS and PS-BC-10R foams. After initial ignition, the specimen showed partial char formation, reduced burning intensity, and self-extinguishing behavior after 22.8 s (t_1) as given in Table 3. Following the second ignition, it self-extinguished after 28 s (t_2). However, localized dripping persisted, and the char structure was fragmented, indicating incomplete barrier development. The moderate increase in LOI (22%) and the delayed flame extinction reflected the combined action of EG expansion and MPP-induced intumescence, although the char produced was mechanically unstable and unable to fully restrain melt dripping or sustain continuous thermal shielding. The slightly uneven outer surface observed for the PS-EG-MPP-BC-10R sample prior to burning could be attributed to die-exit flow effects during extrusion. This behavior is possibly associated with the combined influence of increased melt viscosity at high filler loading and the die geometry (height ratio) of the slit die used.[55] The most pronounced flame retardancy was observed for PS-EG-MPP-BC-10R. This composite ignited only briefly and extinguished rapidly following flame removal, with afterflame times of 6.9 s (t_1) and 12.5 s (t_2), resulting in the shortest maximum afterflame duration among all tested materials. No molten dripping was observed, and a thick, coherent char column remained attached to the specimen throughout combustion. The high LOI value (25%) further confirmed the superior resistance of this formulation to combustion in oxygen-rich environments.

In comparison, both the commercial insulation materials (Foamular NGX C-200 and DuroSpan GPS) displayed persistent dripping and sustained burning behaviors. Foamular NGX burnt fully after 7.5 s during the first flame exposure and exhibited extensive melt dripping alongside an LOI of 20%, indicating limited condensed-phase protection. DuroSpan GPS demonstrated even inferior performance, burning after only 3 s yet exhibiting vigorous dripping and no self-extinguishing capability, despite a comparatively higher LOI of 24%. The extensive dripping observed for both commercial foams suggested insufficient char stabilization and inferior melt-flow suppression relative to the PS-EG-MPP-BC-10R composite foam. Notably, although DuroSpan

Table 3. Torch vertical burning test and LOI test results of PS and fire-retardant composite foams

Sample	Dripping	t_1 (s)	t_2 (s)	Max. afterflame time (s)	Self-extinguishing?	LOI (%)
Pristine PS	Yes	>30	—	>30	No	18
PS-BC-10R	Yes	>30	—	>30	No	20
PS-EG-MPP-10R	Yes (after second ignition)	22.8	28	28	Yes (after first ignition)	22
PS-EG-MPP-BC-10R	No	6.9	12.5	12.5	Yes	25
Foamular NGX C-200	Yes	10	—	10	No	20
DuroSpan GPS	Yes	3	—	3	No	24

t_1 and t_2 represent afterflame durations following the first and second ignition periods, respectively. Maximum afterflame time is reported as the greater of t_1 and t_2 for each specimen, consistent with standard flammability evaluation practice.

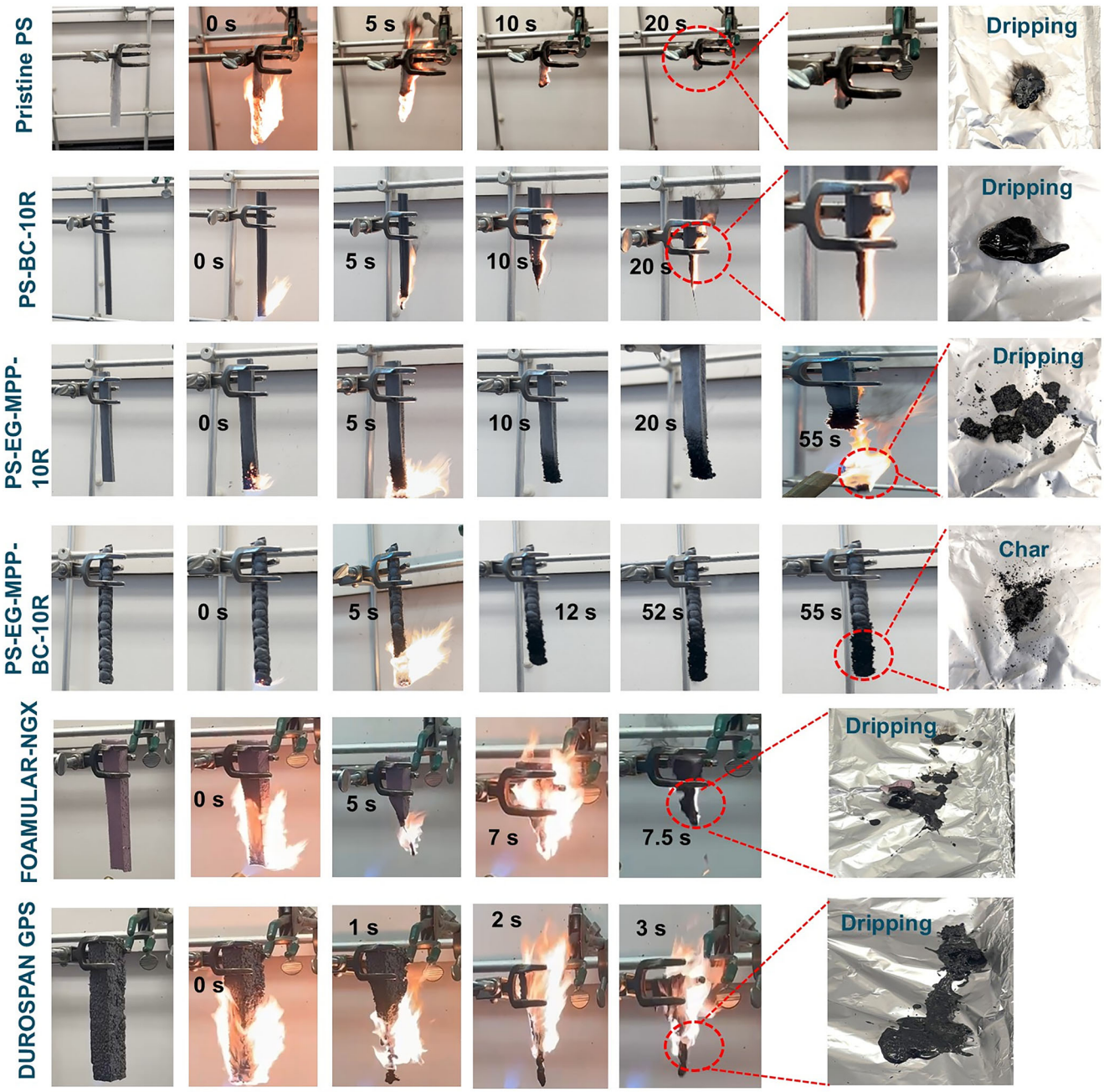

Figure 8. Digital images of torch vertical burning tests for PS composite foams and conventional PS foam insulation materials recorded at selected time intervals during flame exposure and post-flame burning.

Polymer International published by John Wiley & Sons Ltd on behalf of Society of Chemical Industry.

GPS echibited a near-comparable LOI to the PS ternary composite system, the absence of an expanded, mechanically robust char layer resulted in poor flame containment and ineffective condensed-phase flame retardancy. Overall, the torch vertical burning tests demonstrated that only the combination of EG, MPP, and BC delivered comprehensive flame-retardant functionality, manifested by suppressed dripping, stable char formation, rapid self-extinguishing behavior, and maximized oxygen resistance. These results confirmed the exceptional flame-retardant efficacy of PS-EG-MPP-BC-10R relative to both laboratory controls and commercial insulation benchmarks.

Char residue analysis

The chemical structure and graphitic order of the char residues obtained after the torch vertical burning tests were analyzed using FTIR spectroscopy, Raman spectroscopy, and SEM (Figs S1 and 9). As shown in Fig. S1(a), the FTIR spectra of PS-EG-MPP-10R and PS-EG-MPP-BC-10R exhibited nearly identical features, indicating comparable degradation pathways. Bands at *ca* 2920 cm^{-1} were attributed to residual aliphatic C—H stretching, while peaks near 1600 cm^{-1} corresponded to aromatic C=C skeletal vibrations associated with condensed carbon structures.[56,57] A distinct peak observed at *ca* 1030 cm^{-1} for both samples was assigned to P—O—C stretching vibrations originating from phosphate ester groups produced during MPP decomposition.[58] The persistence of these phosphorus-based functionalities confirmed the active condensed-phase role of MPP in promoting char formation. Both the char residues exhibited similar dominant functional groups in FTIR analysis. Within the resolution limits of FTIR spectroscopy for carbonaceous chars, no major chemical differences were detected, suggesting that BC primarily reinforces the char physically rather than introducing distinct new chemical functionalities.

Raman spectra (Fig. S1(b)) of both chars displayed the characteristic D (*ca* 1350 cm^{-1}) and G (*ca* 1580 cm^{-1}) bands corresponding to disordered carbon and sp^2 graphitic domains, respectively. The small G-band profiles indicated incomplete graphitization, which was expected because the chars were generated during short-duration torch burning under nonequilibrium conditions that limited graphitic ordering. The calculated I_D/I_G ratio decreased slightly from 3.5 for PS-EG-MPP-10R to 3.4 for PS-EG-MPP-BC-10R, suggesting a modest increase in carbon structural ordering and improved char development when BC was incorporated. Further macroscopic and microscopic analyses of char residue after burning tests were also carried out. The digital images of char residues are represented in Fig. S2. The microstructural features of the chars observed by SEM are shown in Fig. 9. The PS-EG-MPP-10R char exhibited typical worm-like expanded EG layers with visible pores and voids, forming a loose, fragmented structure that provided limited barrier integrity. In contrast, the PS-EG-MPP-BC-10R system produced a denser and more coherent char layer in which expanded EG domains were fused and embedded within a continuous carbonaceous matrix. This compact morphology indicated more effective physical stabilization and reduced structural collapse during combustion.

Possible flame-retardant mechanism

Figure 10 presents a possible flame-retardant mechanism to explain improved flame retardancy for foam with EG, MPP, and BC. The combined action of EG, MPP, and BC was consistent with a predominantly condensed-phase, compact char-forming flame-retardant mechanism. Upon heating, EG underwent rapid expansion to form a voluminous worm-like graphitic layer that acted as an initial thermal barrier and reduced heat and mass transfer between the flame and the underlying polymer.[59] MPP thermally decomposed to generate a polyphosphoric species that functioned as dehydrating and crosslinking agents, forming a viscous phosphate network capable of coating polymer degradation products and promoting cohesive char formation.[60] FTIR analysis of the residues confirmed the presence of P—O functionalities characteristic of condensed polyphosphate species, supporting the condensed-phase involvement of MPP in producing a phosphorus-rich binding phase within the char.

With the addition of BC to the EG–MPP system, several combined effects were observed. TGA data showed markedly higher residual mass for the EG–MPP–BC formulation relative to EG–MPP and pristine PS, indicating enhanced condensed-phase stabilization. SEM images of the char residues revealed a more continuous, less porous, and mechanically coherent char layer for the ternary formulation, contrasting with the loosely stacked

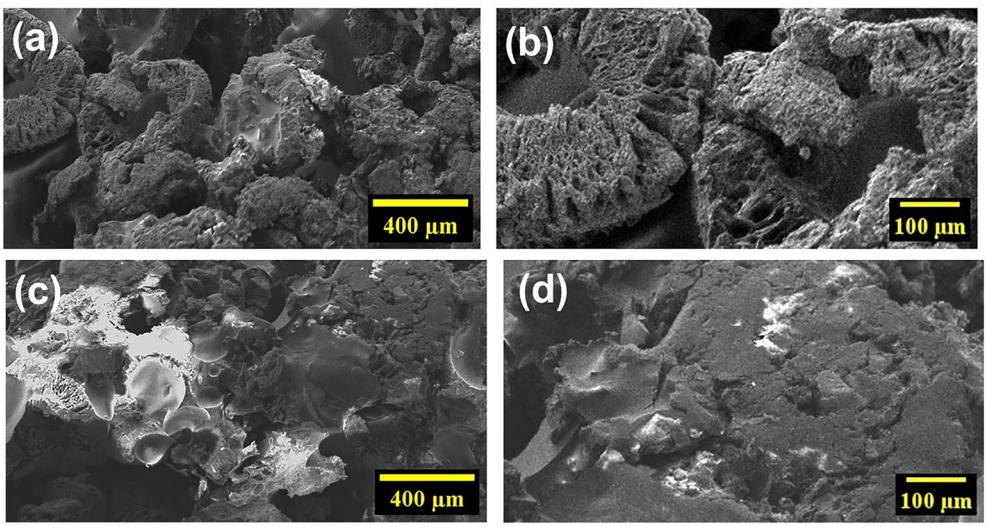

Figure 9. SEM images of char after vertical burning tests: (a, b) PS-EG-MPP-10R; (c, d) PS-EG-MPP-BC-10R.

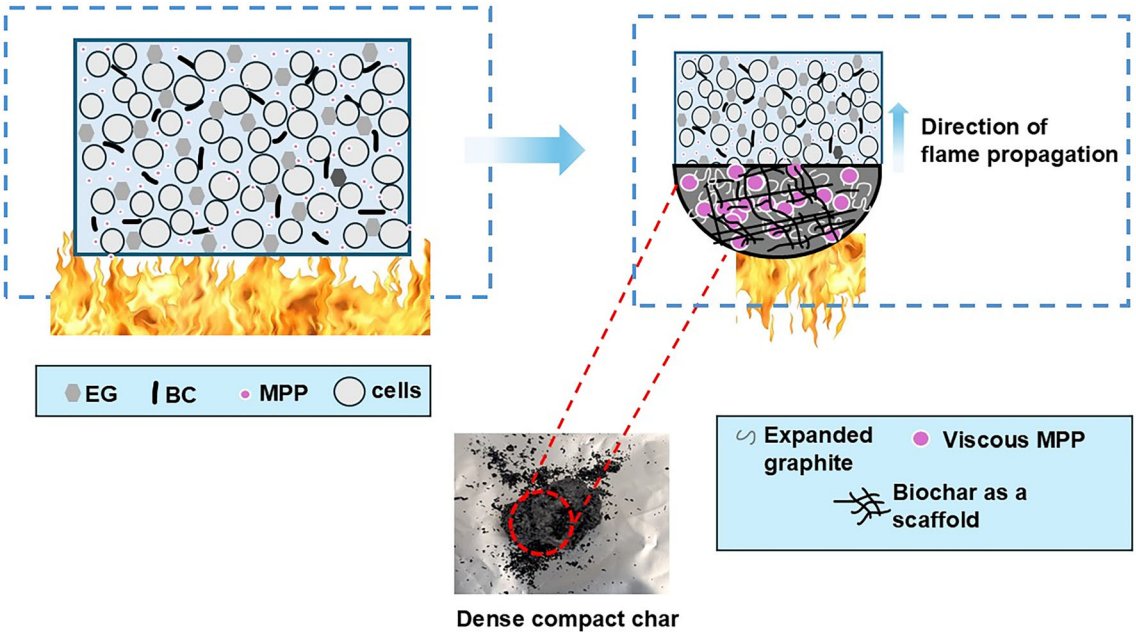

Figure. 10. Schematic of the possible flame-retardant mechanism in PS-EG-MPP-BC-10R foam.

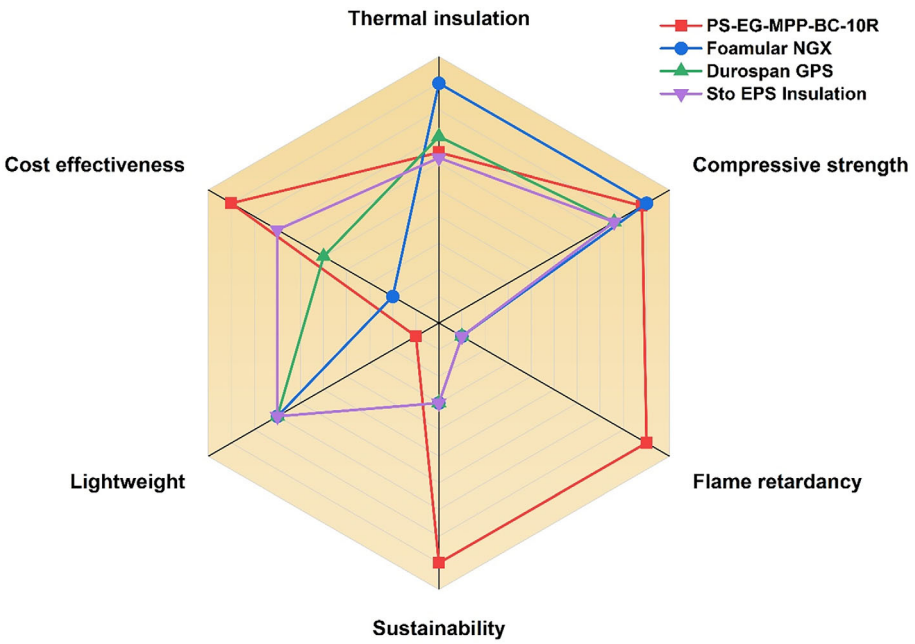

Figure 11. Comparison of comprehensive performance of PS-EG-MPP-BC-10R foam and commercial PS foam insulation boards by a radar chart.

and worm-like expanded EG structure observed in the absence of BC. Raman spectroscopy showed a slight decrease in the I_D/I_G ratio for the EG–MPP–BC residue compared with EG–MPP alone, suggesting a modest increase in the structural ordering of sp^2 carbon domains. This decrease in the I_D/I_G ratio can be interpreted as possibly indicating enhanced carbon organization and stabilization within the char matrix promoted by incorporation of BC. Collectively, the FTIR, Raman, and SEM results demonstrated that MPP provided a viscous polyphosphate binding phase while BC acted as a carbon scaffold and filler that occupied voids between expanded graphite flakes, resulting in a denser, mechanically reinforced char structure. Based on the presented data, BC appeared to function primarily as a mechanical scaffold that densifies and stabilizes the char layer by reinforcing it and thereby interrupting the flame propagation. While this seems to be its dominant role, potential secondary chemical interactions cannot be ruled out without more surface-sensitive analyses. This mechanism most likely could explain the improved torch-burn performance, higher LOI values, reduced mass-loss rates, and increased char yields observed for the PS-EG-MPP-BC-10R composite relative to all other formulations.

Polymer International published by John Wiley & Sons Ltd on behalf of Society of Chemical Industry.

Comparative performance and cost assessment

A comparative assessment of the multifunctional performance and cost effectiveness of the PS-EG-MPP-BC-10R foam against three commercial insulation materials is illustrated in Fig. 11. The hybrid-filler system exhibits strong flame retardancy and superior sustainability due to the inclusion of BC, while also maintaining competitive specific compressive strength. The thermal insulation performance is comparable to that of commercial benchmarks; however, Fig. 9 clearly indicates that further improvement is required in reducing the foam density to enhance its lightweight character and achieve lower thermal conductivity, which are critical attributes for insulation applications. Despite this, the PS-EG-MPP-BC-10R formulation provides a unique balance of mechanical robustness, flame retardancy, and sustainability not simultaneously offered by existing commercial foams. A full, quantitative comparison of all normalized metrics is provided in Table S1 (supporting information). The performance properties of Foamular NGX, DuroSpan GPS, and Sto EPS are taken from their respective technical product datasheets.[61–63]

A comparison of commonly used flame retardants, including traditional mineral and halogenated systems, is provided in Table S2 (supporting information). While mineral-based additives such as aluminium trihydrate and aluminium polyphosphate are relatively low in cost, they require significantly higher loadings to achieve effective flame retardancy. In contrast, the EG–MPP–BC system used in this study achieves comparable performance at lower additive loadings with competitive material cost and improved sustainability.

A retail-price comparison between the developed PS-EG-MPP-BC-10R formulation and representative commercial insulation foams is summarized in Table S3 (supporting information). Based on the method mentioned in supporting information, the projected retail-equivalent cost of PS-EG-MPP-BC-10R is approximately US$4.2 kg^{-1}, which is substantially lower than those of both Foamular NGX[64] (*ca* US$9.5 kg^{-1}) and DuroSpan GPS[65] (*ca* US$11.8 kg^{-1}). As shown in Fig. 11, the PS-EG-MPP-BC-10R formulation exhibits the highest cost-effectiveness among the compared materials, reflecting its significantly lower material cost relative to commercial insulation foams while maintaining superior overall performance. More importantly, this competitive cost is achieved together with markedly improved flame-retardancy performance, including elimination of melt dripping and an LOI of about 25%, as well as clear sustainability benefits arising from the use of BC, recycled PS, and sc-CO_2 as a blowing agent. These results indicate that the PS-EG-MPP-BC-10R formulation offers a favorable balance of cost, flame retardancy, and sustainability for next-generation insulation materials.

CONCLUSIONS

This study demonstrated the successful development of halogen-free, flame-retardant PS foams incorporating EG, MPP, BC, and 10 wt% recycled PS using a pilot-scale sc-CO_2 extrusion process. For the optimized PS-EG-MPP-BC-10R formulation, the combined nucleating effects of EG and BC produced a substantially refined cellular structure, resulting in an approximately 210% increase in cell density (5.8×10^8 cells cm^{-3}) and an approximately 77% reduction in average cell size (50 μm) relative to pristine PS foam. TEM analysis further confirmed that the improved dispersion of carbon-based fillers provided effective heterogeneous nucleation sites, correlating with the enhanced cell density and controlled cellular morphology. Rheological measurements showed an increase in melt viscosity and elastic response with filler incorporation, which contributed to improved melt strength and supported stable cell growth during foaming. These structural enhancements translated directly into mechanical improvements, with the composite exhibiting an approximately 90% higher specific compressive strength (4.63 MPa g^{-1} cm^3) compared with pristine PS, while achieving a thermal conductivity of 39 mW m^{-1} K^{-1}. These results highlight that, despite the high overall filler content (*ca* 11 wt%), the optimized formulation successfully balanced foamability, rigidity, and nucleation behavior to achieve superior structural performance.

Flame-retardancy evaluations further confirmed the strong fire-protection capability of the ternary system. The PS-EG-MPP-BC-10R foam achieved self-extinguishing behavior in torch vertical burning tests with reduced afterflame times, and its LOI value increased to 25%. The substantially higher char yield observed in TGA, together with the compact and mechanically coherent char morphology revealed by SEM, indicated that the primary protection arose from a condensed-phase barrier mechanism. The possible mechanism suggested that EG expanded to form an insulating graphitic layer, MPP generated polyphosphate structures that aided char cohesion, and BC acted as a reinforcing carbon scaffold that densified the protective residue. Collectively, the optimized formulation delivered significant gains in flame retardancy, mechanical robustness, and structural refinement, demonstrating a viable pathway for producing high-performance, halogen-free PS foams using sustainable carbon fillers and industrially relevant processing conditions.

ACKNOWLEDGEMENTS

The authors acknowledge the financial support from Western Sustainable Impact Fund (WSIF), Mitacs, NSERC CREATE (grant number 401209347) and NSERC Discovery grants. The authors gratefully acknowledge Dr. Abdul Mumin from Lambton College, Sarnia, Ontario, Canada, for his valuable assistance with rheological testing and data processing.

DATA AVAILABILITY STATEMENT

The data that support the findings of this study are available from the corresponding author upon request.

CONFLICTS OF INTEREST

There are no conflicts to declare.

AUTHOR CONTRIBUTIONS

Apurv Gaidhani: Conceptualization, methodology, experimentation, investigation, data curation, formal analysis, visualization, writing – original draft. Harasavardanan Velumani Jayaraman: Data curation, writing – review and editing, validation. Stephan Edwards: Investigation, experimentation, data curation. Lauren Tribe: Supervision, methodology, validation, funding acquisition, writing – review and editing. Paul Charpentier: Supervision, conceptualization, methodology, funding acquisition, writing – review and editing.

SUPPORTING INFORMATION

Supporting information may be found in the online version of this article.

REFERENCES

1 Wang G, Li W, Bai S and Wang Q, *ACS Omega* **4**:9306–9315 (2019). https://doi.org/10.1021/acsomega.9b00321.
2 Expanded Polystyrene Environmental Profile (2024). https://globaleps.org/wp-content/uploads/2023/11/gesa-environmental-profile-april-2024.pdf (Accessed 24 April 2026).
3 Amirabadi S, Ramezani Kakroodi A, Dias OAT, Sain M and Park CB, *Mater Des* **214**:110419 (2022). https://doi.org/10.1016/j.matdes.2022.110419.
4 Rao WH, Zhu ZM, Wang SX, Wang T, Tan Y, Liao W *et al.*, *Polym Degrad Stab* **153**:192–200 (2018). https://doi.org/10.1016/j.polymdegradstab.2018.04.029.
5 The Critical Role of Buildings (2019). https://www.iea.org/reports/the-critical-role-of-buildings (Accessed 5 April 2026).
6 Gaidhani A, Min G, Xu WZ, Tribe L and Charpentier P, *Polym Eng Sci* **65**:4170–4185 (2025). https://doi.org/10.1002/pen.27283.
7 Ürge-Vorsatz D, Cabeza LF, Serrano S, Barreneche C and Petrichenko K, *Renew Sustain Energy Rev* **41**:85–98 (2015). https://doi.org/10.1016/j.rser.2014.08.039.
8 Yan YW, Huang JQ, Guan YH, Shang K, Jian RK and Wang YZ, *Polym Degrad Stab* **99**:35–42 (2014). https://doi.org/10.1016/j.polymdegradstab.2013.12.014.
9 Wang G and Bai S, *J Appl Polym Sci* **134**:45474 (2017). https://doi.org/10.1002/app.45474.
10 Chan YY and Schartel B, *Polymers* **14**:2562 (2022). https://doi.org/10.3390/polym14132562.
11 Gao L, Zheng G, Zhou Y, Hu L, Feng G and Zhang M, *Polym Degrad Stab* **101**:92–101 (2014). https://doi.org/10.1016/j.polymdegradstab.2013.12.025.
12 Gaidhani A, Tribe L and Charpentier P, *J Cell Plast* **59**:419–453 (2023). https://doi.org/10.1177/0021955X231215753.
13 Khanal S, Zhang W, Ahmed S, Ali M and Xu S, *Compos Part A Appl Sci Manuf* **112**:444–451 (2018). https://doi.org/10.1016/j.compositesa.2018.06.030.
14 Lim KS, Bee ST, Sin LT, Tee TT, Ratnam CT, Hui D *et al.*, *Compos Part B Eng* **84**:155–174 (2016). https://doi.org/10.1016/j.compositesb.2015.08.066.
15 Global Plastics Outlook (2022). https://doi.org/10.1787/de747aef-en.
16 Economic Study of the Canadian Plastic Industry (2019). https://publications.gc.ca/collections/collection_2019/eccc/En4-366-1-2019-eng.pdf.
17 Matthews C, Moran F and Jaiswal AK, *J Clean Prod* **283**:125263 (2021). https://doi.org/10.1016/j.jclepro.2020.125263.
18 Liu W, Wu X, Qiu W, Li Y, Jia S and Xiao L, *Polym Int* **75**:80–92 (2026). https://doi.org/10.1002/pi.70034.
19 Liu W, Wu X, Qiu W, Li Y, Jia S and Xiao L, *Polym Eng Sci* **65**:4682–4694 (2025). https://doi.org/10.1002/pen.70002.
20 Liu W, Wu X, Liu J, Lu F, Li Y, Jia S *et al.*, *Langmuir* **42**:1234–1245 (2026). https://doi.org/10.1021/acs.langmuir.5c05310.
21 Bartoli M, Arrigo R, Malucelli G, Tagliaferro A and Duraccio D, *Polymers* **14**:2506 (2022). https://doi.org/10.3390/polym14122506.
22 Das O, Mensah RA, Balasubramanian KBN *et al.*, *Compos Part C: Open Access* **11**:100368 (2023). https://doi.org/10.1016/j.jcomc.2023.100368.
23 Wang M, Yin GZ, Yang Y, Fu W, Díaz Palencia JL, Zhao J *et al.*, *Adv Ind Eng Polym Res* **6**:132–155 (2023). https://doi.org/10.1016/j.aiepr.2022.07.003.
24 Gaidhani A, Edwards S, Xu WZ, Tribe L and Charpentier P, *J Appl Polym Sci* **143**:e70441 (2026). https://doi.org/10.1002/app.70441.
25 Gaidhani A, Min G, Tribe L and Charpentier P, *RSC Sustain* **4**:996–1008 (2025). https://doi.org/10.1039/D5SU00884K.
26 Mensah RA, Wang D, Shanmugam V, Sas G, Försth M and das O, *Compos Part C: Open Access* **14**:100471 (2024). https://doi.org/10.1016/j.jcomc.2024.100471.
27 Das O, Bhattacharyya D, Hui D and Lau KT, *Compos Part B Eng* **106**:120–128 (2016). https://doi.org/10.1016/j.compositesb.2016.09.020.
28 Jin FL, Zhao M, Park M and Park SJ, *Polymers* **11**:953 (2019). https://doi.org/10.3390/polym11060953.
29 Sun H, Chen K, Liu Y and Wang Q, *Eur Polym J* **192**:112148 (2023). https://doi.org/10.1016/j.eurpolymj.2023.112148.
30 Zafar MT, Kumar S, Singla RK, Maiti SN and Ghosh AK, *Fibers Polym* **19**:648–659 (2018). https://doi.org/10.1007/s12221-018-7428-4.
31 Bhagat AB, Pal R and Ghosh AK, *Polym Compos* **45**:555–568 (2024). https://doi.org/10.1002/pc.27797.
32 Sorrentino L, Aurilia M, Cafiero L, Cioffi S and Iannace S, *J Cell Plast* **48**:355–368 (2012). https://doi.org/10.1177/0021955X12449641.
33 Yousefzade O, Hemmati F, Garmabi H and Mahdavi M, *Express Polym Lett* **9**:932–944 (2015).
34 Haham H, Riscoe A, Frank CW and Billington SL, *Appl Surf Sci Adv* **3**:100059 (2021). https://doi.org/10.1016/j.apsadv.2021.100059.
35 Uram K, Kurańska M, Andrzejewski J and Prociak A, *Materials* **14**:5616 (2021). https://doi.org/10.3390/ma14195616.
36 Acuña P, Li Z, Santiago-Calvo M, Villafañe F, Rodríguez-Perez MÁ and Wang DY, *Polymers* **11**:168 (2019). https://doi.org/10.3390/polym11010168.
37 Hu Y, Zhou Z, Li S, Yang D, Zhang S and Hou Y, *Front Mater* **7**:629284 (2021). https://doi.org/10.3389/fmats.2020.629284.
38 Najafi N, Heuzey MC, Carreau PJ, Therriault D and Park CB, *Rheol Acta* **53**:779–790 (2014). https://doi.org/10.1007/s00397-014-0801-3.
39 Raps D, Köppl T, De Anda AR and Altstädt V, *Polymer* **55**:1537–1545 (2014). https://doi.org/10.1016/j.polymer.2014.01.036.
40 Mihai M, Huneault MA and Favis BD, *Polym Eng Sci* **50**:629–642 (2010). https://doi.org/10.1002/pen.21561.
41 Cuthbertson D, Berardi U, Briens C and Berruti F, *Biomass Bioenergy* **120**:77–83 (2019). https://doi.org/10.1016/j.biombioe.2018.11.007.
42 Park C, Gong P *et al.*, SPE ANTEC Proceedings (2016). https://www.proceedings.com/content/052/052412webtoc.pdf.
43 Gong P, Buahom P, Tran MP, Saniei M, Park CB and Pötschke P, *Carbon* **93**:819–829 (2015). https://doi.org/10.1016/j.carbon.2015.06.003.
44 Chen J, Yang L, Chen D, Mai Q, Wang M, Wu L *et al.*, *Cell Polym* **40**:101–118 (2021). https://doi.org/10.1177/0262489320930328.
45 Gaidhani A, Edwards S, Tribe L and Charpentier P, *J Thermoplast Compos Mater* **39**:1–23 (2025). https://doi.org/10.1177/08927057251401189.
46 Schnabel W, Levchik GF, Wilkie C, Wilkie CA, Jiang DD and Levchik SV, *Polym Degrad Stab* **63**:365–375 (1999). https://doi.org/10.1016/S0141-3910(98)00114-1.
47 Alghyamah AA, Yagoub Elnour A, Shaikh H, Haider S, Manjaly Poulose A, al-Zahrani SM *et al.*, *J King Saud Univ Sci* **33**:101409 (2021). https://doi.org/10.1016/j.jksus.2021.101409.
48 Li Z, Zhang Q, Cui J and Yan Y, *Materials* **18**:4308 (2025). https://doi.org/10.3390/ma18184308.
49 Liu J, Zhang Y, Peng S, Pan B, Lu C, Liu H *et al.*, *Polym Degrad Stab* **121**:261–270 (2015). https://doi.org/10.1016/j.polymdegradstab.2015.09.018.
50 Huang X, Chen G, Zhou Z, Hu J, Wang C and Chen D, *Case Stud Therm Eng* **28**:101623 (2021). https://doi.org/10.1016/j.csite.2021.101623.
51 Ohlemiller TJ, Shields JR Natl. Inst. Stand. Technol. Tech. Note 1493 (2008) https://doi.org/10.6028/NIST.TN.1493
52 Zhou B, Yoshioka H, Noguchi T and Ando T, *Therm Sci Eng Prog* **8**:83–92 (2018). https://doi.org/10.1016/j.tsep.2018.08.002.
53 Li ME, Yan YW, Zhao HB, Jian RK and Wang YZ, *Compos Part B* **185**:107797 (2020). https://doi.org/10.1016/j.compositesb.2020.107797.
54 Zhu ZM, Rao WH, Kang AH, Liao W and Wang YZ, *Polym Degrad Stab* **154**:1–9 (2018). https://doi.org/10.1016/j.polymdegradstab.2018.05.015.
55 Esposito C, Trofa M, Tammaro D, Lombardi L, D'Avino G and Maffettone PL, *J Manuf Process* **160**:99–110 (2026). https://doi.org/10.1016/j.jmapro.2026.01.073.
56 Tai Q, Yuen RKK, Yang W, Qiao Z, Song L and Hu Y, *Compos Part A Appl Sci Manuf* **43**:415–422 (2012). https://doi.org/10.1016/j.compositesa.2011.10.012.
57 Pan Y, Luo Z and Wang B, *Polymers* **12**:2761 (2020). https://doi.org/10.3390/polym12112761.
58 Spevak L, Flach CR, Hunter T, Mendelsohn R and Boskey A, *Calcif Tissue Int* **92**:418–428 (2013). https://doi.org/10.1007/s00223-013-9695-9.
59 Khalili P, Tshai KY and Kong I, *Compos Part A Appl Sci Manuf* **100**:194–205 (2017). https://doi.org/10.1016/j.compositesa.2017.05.015.
60 Su M, Duo Y, Chen S, Jiang B, Ding D, Li J *et al.*, *Fuel* **401**:135800 (2025). https://doi.org/10.1016/j.fuel.2025.135800.
61 DuroSpan® GPS R5 Insulation https://www.plastifab.com/products/durospan-gps-insulation/durospan-gps-r5.html [19 April 2026].
62 Sto EPS Insulation Board Product Bulletin https://www.stocorp.com/wp-content/content/Products_TechService/Insulation/Product%20Bulletins/PB_5782430_Sto%20EPS%20Insulation%20Board_EN.pdf [9 March 2026].
63 FOAMULAR NGX Technical Data Sheet (2020). https://www.owenscorning.com/en-ca/technical-resource-library/products/foamular-ngx [10 April 2026].
64 Owens Corning FOAMULAR NGX (2026). https://www.homedepot.ca/product/owens-corning-foamular-ngx-c-300-xps-rigid-foam-insulation-board-2-inch-x-24-inch-x-96-inch-r-10-sl-edge/1000155124 [19 April 2026].
65 DuroSpan GPS R10 (2026). https://www.homedepot.ca/product/durospan-gps-r10-2-13-inch-x-48-inch-x-96-inch-r-value-10-gps-rigid-insulation-foam-board/1001211235 [28 April 2026].

Polymer International published by John Wiley & Sons Ltd on behalf of Society of Chemical Industry.